

Lie Algebra-Based Quantum Optimal Controls Interpolation

Piero Luchi^{1,2,*} and Francesco Pederiva^{1,2}

¹*Dipartimento di Fisica, University of Trento, via Sommarive 14, I-38123, Povo, Trento, Italy*

²*INFN-TIFPA Trento Institute of Fundamental Physics and Applications, Trento, Italy*

We present a framework combining Lie group theory and feed-forward neural networks to efficiently generate quantum optimal control pulses for arbitrary unitary operations in superconducting qubit systems, bypassing the need for explicit optimization at inference time. The exponential scaling of the Hilbert space dimension with qubit number makes standard optimization approaches computationally prohibitive when large ensembles of distinct propagators must be processed, a bottleneck that is particularly acute in Trotterized quantum simulation. Our method addresses this limitation by pre-computing a representative set of control pulses via Lie group theory and training neural networks to map target propagators to their corresponding pulses. We demonstrate the approach on superconducting qubit systems of 2, 3, and 4 qubits, finding high reconstruction fidelity for specific combinations of Lie algebra parameters. As a physically motivated benchmark, we apply the methodology to reconstruct control pulses for the Trotter propagators of a neutrino system undergoing collective flavor oscillations. The successful generalization across system types demonstrates that a single model – trained once on hardware-specific random propagators – can serve as a universal control-pulse generator for any target quantum system of compatible Hilbert space dimension, offering a promising route toward scalable quantum simulation.

I. INTRODUCTION

Implementing a generic unitary operation in a quantum computer usually relies on its decomposition into a sequence of one and two-qubit unitary basis operations [1]. This approach is based on the well-known Solovay–Kitaev theorem [2], stating that the number of elements into which a given unitary operation can be approximated by decomposing it in a set of elementary operations scales reasonably with its size. Despite this property, quantum circuits resulting from such decomposition often are too deep for being run in a time shorter than the typical decoherence time of the present day qubits. This results in the accumulation of errors that individual basic operations introduce in the whole circuit, eventually spoiling the result.

Quantum optimal control (QOC) techniques [3, 4] were applied to this field as a possible route to reduce this error accumulation. QOC helps to steer the time evolution of a quantum systems (i.e. the qubits) to realize the desired unitary operation. This is obtained by optimizing a set of external control pulses, coupled to the quantum system via control operators, such that they drive the system according to the desired unitary. This allows to implement arbitrary unitary operations in a minimal number of applications, reducing the duration of transformation and therefore the overall accumulation of error. Two caveats are in order. First, QOC presupposes accurate knowledge of the system Hamiltonian, an assumption that is non-trivial in practice. Second, the flexibility of the approach comes at a computational cost that scales exponentially with the number of qubits, i.e. with the Hilbert-space dimension, a limitation that QOC shares with the gate-decomposition approach.

The cost of QOC becomes particularly limiting in the context of digital quantum simulation. The Lloyd construction [5], together with its higher-order Trotter–Suzuki refinements [6], expresses the time evolution generated by a many-body Hamiltonian as a product of short-time propagators, one for each Trotter step. A single simulation run therefore requires the realization of a large number of *distinct* unitaries, and exploring different evolution times, Hamiltonian parameters, or physical observables multiplies this count further. Re-running a full optimal-control routine independently for every target is impractical, and motivates the search for methods that, after the optimization of a representative set of pulses performed once and for all, can produce the control sequence for any new target unitary at negligible additional cost.

A natural strategy to address this bottleneck is to combine QOC with machine learning. Reinforcement learning has been shown to discover control protocols competitive with, or in some regimes superior to, gradient-based optimizers for both state preparation [7] and gate synthesis [8], while gradient-based and chopped-basis schemes such as GRAPE [9, 10] and CRAB [11] remain the standard workhorses for the underlying single-target optimization. More recent work has begun to address the multi-target setting directly: Sauvage and Mintert [12] optimize a single parametrized pulse family across a continuous set of target gates, and pulse-level perspectives on variational quantum algorithms [13] highlight the value of recycling control resources across related tasks. What is still largely missing is a framework that (i) exploits the group-theoretic structure of the target unitaries to define a representative training set in a principled way, and (ii) treats the map from target propagator to control pulses as a regression problem that can be amortized once and reused across physically distinct simulation tasks.

In this work we propose such a framework, which

* piero.luchi@unitn.it

we call Lie Algebra-based Control Pulse Reconstruction (LA-CPR). The starting observation is that every N_q -qubit propagator belongs to the compact Lie group $SU(N)$, which can be sampled systematically through its Lie algebra $\mathfrak{su}(N)$ expressed in the Pauli tensor basis. We restrict the sampling to a tractable subset of generators corresponding to a linear chain topology with Ising ZZ couplings – understood here as a restriction on the unitaries to be synthesized rather than as a constraint on the underlying hardware – and draw random elements from a neighborhood of the group identity. For each sampled propagator a control pulse is optimized once via GRAPE [9, 10], building a dataset of propagator-pulse pairs. Two feed-forward neural networks are then trained to regress the in-phase and quadrature components of the control envelope from the matrix entries of the target unitary, so that at inference time the controls for any new target are obtained by a single network evaluation, with no further optimization required. We validate the method on superconducting qubit systems of $N_q = 1-4$ qubits and, as a physically motivated benchmark, we apply it to the Trotter propagators of neutrino collective flavor oscillations [14, 15], showing that a network trained on hardware-generic samples generalizes to a quantum simulation task it has never seen during training, building on and extending our earlier work on pulse reconstruction [16, 17].

II. METHODS

A. Quantum Optimal Control

The general Hamiltonian of a qubit system is:

$$H_{QC} = H_0 + \sum_{k=1}^{N_{ctrl}} \epsilon_k(t) H_k. \quad (1)$$

H_0 is the drift term of the Hamiltonian, and it depends on the physical properties of the device as the type of qubits (trapped ions, superconducting, etc.), their couplings and connectivity. H_k are the drive Hamiltonians that describe how the external environment can interact with the system. The modulation in time of the strength of these drive Hamiltonians is described by the N_{ctrl} functions $\epsilon_k(t)$. The number N_{ctrl} of such controls depends on the specific hardware and the connectivity between the qubits.

The time-evolution of the system during a time step t_j of the pulses is given by the propagator:

$$U_{t_j} = \exp \left\{ -i \left(H_0 + \sum_{k=1}^{N_{ctrl}} \epsilon_k(t_j) H_k \right) \Delta t \right\}, \quad (2)$$

hence the system's state $|\psi(t)\rangle$ at the final time t_N is:

$$|\psi(t_N)\rangle = U_{t_N} U_{t_{N-1}} \dots U_{t_2} U_{t_1} |\psi(t_0)\rangle. \quad (3)$$

The complete propagator is therefore:

$$U = U_{t_N} U_{t_{N-1}} \dots U_{t_2} U_{t_1} = \mathcal{T} \exp \left\{ -i \left(H_0 + \sum_{j=0}^N \sum_{k=1}^{N_{ctrl}} \epsilon_k(t_j) H_k \right) \Delta t \right\}, \quad (4)$$

where $\mathcal{T} \exp\{\}$ stands for time-ordered exponential. The optimal control problem consists in finding the best control shapes $\epsilon_k(t)$ such that, when applied to the quantum device for a total time t_N , drive the system from the state $|\psi(0)\rangle$ to the desired state $|\psi(t_N)\rangle$ within an acceptable error.

Among the great amount of optimization procedure, in this work Gradient Ascend Pulse Engineering (GRAPE) [9, 10] procedure is used. In particular, given a target operator U_{target} (that drives the quantum system state in the desired way), the optimal set of controls are found by adjusting their single time-steps $\epsilon_k(t_j) \forall k \in [0, N_{ctrl}], j \in [0, N]$ while maximizing the cost function called *fidelity* \mathcal{F} :

$$\mathcal{F} = 1 - \tilde{\mathcal{D}}, \quad (5)$$

where $\tilde{\mathcal{D}}$ is the normalized Hilbert-Schmidt norm,

$$\tilde{\mathcal{D}} = \frac{1}{2} - \frac{1}{2d} \text{Re} \text{Tr}(U_{target}^\dagger U_0(\tau)), \quad (6)$$

with $d = \dim(U_{target})$ the dimension of the matrices. This metric quantifies the similarity of the two matrices by giving a value close to one when they are similar and close to zero when they are different. So we need to solve the general optimization problem:

$$\{\epsilon_k^*(t_j)\} = \arg \max_{\{\epsilon_k(t_j)\}} \mathcal{F}(U_{target}, U(\{\epsilon_k(t_j)\})). \quad (7)$$

The optimal control framework outlined above is general and applies to any form of the qubit Hamiltonian H_0 . In the next subsection (Sec. II B) we specialize it to the hardware considered in this work: a system of N_q superconducting qubits coupled to a common cavity bus resonator, operated in the dispersive regime and driven by a global microwave control field [18–21].

B. Qubits System

We now specialize the general control Hamiltonian of Eq. (1) to the hardware considered in this work, by deriving the effective qubit Hamiltonian below.

The starting point is the generalized Tavis-Cummings model [22] within the rotating-wave approximation (RWA) [20]. By assuming that the detuning between the qubits and the cavity mode is much larger than their respective coupling strengths, i.e., $|\omega_k - \omega_c| \gg g_k$, we can perturbatively eliminate the cavity degrees of freedom using a Schrieffer-Wolff transformation [20]. In this

dispersive regime, direct energy exchange between the qubits and the cavity is suppressed. Instead, the cavity mediates virtual photon exchanges, which manifest as an always-on effective transverse interaction (XY -type exchange) between the qubits [23, 24].

To describe the driven dynamics, we move into a frame rotating at the angular frequency of the global microwave drive, ω_d . In this rotating frame, the fast oscillating terms of the control field are eliminated, leaving only the slowly varying pulse envelopes [25]. The drift, interaction, and control terms of Eq. (1) take then the explicit form:

$$\hat{H}_{QC}(t) = H_{\text{drift}} + H_{\text{int}} + H_{\text{ctrl}}(t), \quad (8)$$

where the drift, interaction, and control Hamiltonians are given by:

$$H_{\text{drift}} = \sum_{k=1}^{N_q} \frac{\Delta_k}{2} \sigma_z^{(k)}, \quad (9)$$

$$\begin{aligned} H_{\text{int}} &= \sum_{\langle j,k \rangle} J_{jk} \left(\sigma_+^{(j)} \sigma_-^{(k)} + \sigma_-^{(j)} \sigma_+^{(k)} \right) \\ &= \sum_{\langle j,k \rangle} \frac{J_{jk}}{2} \left(\sigma_x^{(j)} \sigma_x^{(k)} + \sigma_y^{(j)} \sigma_y^{(k)} \right), \end{aligned} \quad (10)$$

$$\begin{aligned} H_{\text{ctrl}}(t) &= \frac{1}{2} \Omega_x(t) \sum_{k=1}^{N_q} \lambda_k \sigma_x^{(k)} \\ &\quad + \frac{1}{2} \Omega_y(t) \sum_{k=1}^{N_q} \lambda_k \sigma_y^{(k)}. \end{aligned} \quad (11)$$

Here, N_q is the number of qubits. The operators $\sigma_{x,y,z}^{(k)}$ are the standard Pauli matrices acting on the k -th qubit, with raising and lowering operators defined as $\sigma_+^{(k)} = |1\rangle\langle 0|$ and $\sigma_-^{(k)} = |0\rangle\langle 1|$. Throughout this work we adopt natural units with $\hbar = 1$.

The drift Hamiltonian H_{drift} describes the free precession of each qubit in the rotating frame, where $\Delta_k = \omega_k - \omega_d$ is the detuning between the bare transition frequency ω_k of the k -th qubit and the global drive frequency ω_d . In this work, the drive frequency ω_d is chosen to be the average qubit frequency, $\omega_d = \frac{1}{N_q} \sum_{k=1}^{N_q} \omega_k$, to minimize the maximum detuning across the register.

The interaction Hamiltonian H_{int} captures the exchange-type coupling between pairs of qubits, mediated by dispersive interaction with the cavity. The coupling rate J_{jk} quantifies the effective flip-flop interaction strength between qubits j and k . The sum runs over nearest-neighbor pairs in the connectivity graph of the device: the angle-bracket notation $\langle j, k \rangle$ denotes an unordered pair of neighboring qubits, so each interacting pair is counted exactly once. In this work, we assume a chain topology for the qubit connectivity.

The control Hamiltonian $H_{\text{ctrl}}(t)$ represents the action of the global microwave drive on the qubit register. The time-dependent envelopes $\Omega_x(t)$ and $\Omega_y(t)$ are the slowly

varying Rabi frequencies corresponding to the in-phase (I) and quadrature (Q) components of the pulse, respectively. The dimensionless coefficient λ_k accounts for the relative coupling strength of the global drive field to each individual qubit, which may differ due to variations in the physical layout of the device. For simplicity, we set $\lambda_k = 1$ for all k throughout this work.

C. Lie Groups and Algebras

A *Lie group* G is a finite-dimensional smooth manifold endowed with a smooth group structure. Its associated *Lie algebra* \mathfrak{g} is the space of infinitesimal generators of the group, connected to G through the *exponential map* $\exp : \mathfrak{g} \rightarrow G$, which allows any group element to be written as $U(\gamma) = \exp\{i\gamma \cdot T\}$, where the generators $T_p = -i \partial U / \partial \gamma_p |_{\gamma \rightarrow 0} \text{span } \mathfrak{g}$ [26].

In the context of an N_q -qubit system, the relevant group is the special unitary group $SU(N)$, where $N \equiv 2^{N_q}$ denotes the dimension of the Hilbert space. $SU(N)$ is the group of $N \times N$ unitary matrices with determinant 1; it is a real Lie group of dimension $N^2 - 1$, whose Lie algebra $\mathfrak{su}(N)$ consists of traceless anti-Hermitian $N \times N$ matrices. Any unitary transformation U acting on N_q qubits belongs to $SU(N)$ and can be written as the exponential of its generator in $\mathfrak{su}(N)$ [26, 27]:

$$U = \exp(-iH) \in SU(N), \quad (12)$$

$$H = \sum_{k=1}^{N^2-1} \gamma_k T_k \in \mathfrak{su}(N), \quad (13)$$

where $\{T_k\}_{k=1}^{N^2-1}$ form an orthonormal basis of $\mathfrak{su}(N)$ with respect to the Hilbert-Schmidt inner product, satisfying [28, 29]

$$\text{Tr}(T_j^\dagger T_k) = N \delta_{jk}. \quad (14)$$

The parameters γ_k are *free real numbers* with periodicity 2π , since

$$e^{-i(\gamma_k + 2\pi)T_k} = e^{-i\gamma_k T_k}, \quad (15)$$

which follows directly from $T_k^2 = \mathbb{I}$ and the identity $e^{-i\gamma T} = \cos(\gamma) \mathbb{I} - i \sin(\gamma) T$ [27]. The natural fundamental domain is therefore $\gamma_k \in (-\pi, +\pi]$, symmetric about the origin. The exponential map $\exp : \mathfrak{su}(N) \rightarrow SU(N)$ is surjective [30] (since $SU(N)$ is compact and connected) but not injective: parameter values differing by integer multiples of 2π yield the same unitary.

1. Pauli Tensor Basis Decomposition

The generators T_k are all tensor products of Pauli matrices $\{\mathbb{I}, \sigma_x, \sigma_y, \sigma_z\}^{\otimes N_q}$ excluding $\mathbb{I}^{\otimes N_q}$, and are naturally classified by their *locality* ℓ , i.e., the number of

qubits on which they act non-trivially [28, 29]. The Hamiltonian takes the explicit form

$$H = \sum_{\ell=1}^{N_q} \sum_{i_1 < \dots < i_\ell} \sum_{a_1, \dots, a_\ell} \gamma_{a_1 \dots a_\ell}^{(i_1 \dots i_\ell)} \sigma_{a_1}^{(i_1)} \otimes \dots \otimes \sigma_{a_\ell}^{(i_\ell)}, \quad (16)$$

with $a_j \in \{x, y, z\}$. The number of ℓ -qubits terms is $\binom{N_q}{\ell} \cdot 3^\ell$, and summing over all locality levels gives

$$\sum_{\ell=1}^{N_q} \binom{N_q}{\ell} 3^\ell = (1+3)^{N_q} - 1 = 4^{N_q} - 1 = N^2 - 1, \quad (17)$$

which equals the dimension of $\mathfrak{su}(N)$. As the $N^2 - 1$ parameters γ_k range freely over $(-\pi, +\pi]$, Eq. (16) parametrizes the entire group $SU(N)$.

The ℓ -qubits block captures genuinely ℓ -partite correlations, irreducible to lower-order terms. Discarding the N_q -qubits terms, restricts H to a subspace of dimension $N^2 - 1 - 3^{N_q}$, which generates only a *proper subgroup* of $SU(N)$.

TABLE I: Locality structure of the Pauli tensor basis for general N_q .

Locality ℓ	Operators	No. of terms
1-qubits	$\sigma_a^{(i)}$	$3N_q$
2-qubits	$\sigma_a^{(i)} \otimes \sigma_b^{(j)}, i < j$	$9\binom{N_q}{2}$
\vdots	\vdots	\vdots
N_q -qubits	$\sigma_{a_1}^{(1)} \otimes \dots \otimes \sigma_{a_{N_q}}^{(N_q)}$	3^{N_q}
Total		$4^{N_q} - 1$

Example: $N_q = 2, SU(4)$

For $N_q = 2$, the algebra $\mathfrak{su}(4)$ has dimension $4^2 - 1 = 15$ [31, 32]. The Hamiltonian expands as

$$H = \underbrace{\sum_{i=1}^2 \sum_a \gamma_a^{(i)} \sigma_a^{(i)}}_{\text{1-qubits: 6 terms}} + \underbrace{\sum_{a,b} \gamma_{ab} \sigma_a^{(1)} \otimes \sigma_b^{(2)}}_{\text{2-qubits: 9 terms}}. \quad (18)$$

TABLE II: Pauli basis for $N_q = 2, \dim \mathfrak{su}(4) = 15$.

Locality	Operators	No. of terms
1-qubits	$\sigma_a^{(1)}, \sigma_a^{(2)}$	6
2-qubits	$\sigma_a^{(1)} \otimes \sigma_b^{(2)}$	9
Total		15

The analogous decomposition for $N_q = 3$ ($\dim \mathfrak{su}(8) = 63$), which exhibits the additional 3-qubits locality block, is reported in Appendix A.

2. Simplifications in Qubits Chain Topology

In this work, we consider superconducting qubits, which inherently support only nearest-neighbor interactions due to their physical implementation. We impose two successive, physically motivated restrictions on the gate set, each of which reduces the number of free parameters while preserving universality.

a. First simplification: linear chain topology. It is natural to adopt a linear connectivity topology $1-2-\dots-N_q$. Within this architecture, the available native gates act locally and generate the corresponding local operator algebra. Concretely, the single-qubit gates on each site i generate a copy of $\mathfrak{su}(2)^{(i)}$, while the two-qubit entangling gates on each neighboring pair $(i, i+1)$ generate $\mathfrak{su}(4)_{i, i+1}$. The dynamical Lie algebra [33, 34] of the full N_q -qubit chain is therefore

$$\mathfrak{g} = \bigoplus_{i=1}^{N_q} \mathfrak{su}(2)^{(i)} \oplus \bigoplus_{i=1}^{N_q-1} \mathfrak{su}(4)_{i, i+1}, \quad (19)$$

whose dimension is

$$\dim \mathfrak{g} = \underbrace{3N_q}_{\text{single-qubit}} + \underbrace{15(N_q - 1)}_{\text{two-qubit}} = 18N_q - 15. \quad (20)$$

Since $\dim \mathfrak{su}(N) = N^2 - 1$, the inequality $18N_q - 15 < N^2 - 1$ holds for all $N_q \geq 2$, confirming that \mathfrak{g} is *not* the full $\mathfrak{su}(N)$: the native gate set does not span all traceless skew-Hermitian operators on $(\mathbb{C}^2)^{\otimes N_q}$.

Nevertheless, the group generated by \mathfrak{g} is *dense* in $SU(N)$: the missing directions of $\mathfrak{su}(N)$ are recovered via nested Lie brackets of nearest-neighbor generators, which produce effective long-range couplings mediated by the intermediate qubits, so that [34, 35]

$$\overline{\langle e^{\mathfrak{g}} \rangle} = SU(N). \quad (21)$$

An explicit Pauli-string example of this construction is given in Appendix B. The chain topology thus does *not* simplify the general Hamiltonian, but *constrains the connectivity* of elementary gates while preserving universality through iterated nearest-neighbor operations.

b. Second simplification: Ising ZZ coupling. We further simplify the problem by restricting the set of unitaries that the circuit is allowed to implement directly: among the two-qubit primitives, we retain only rotations generated by $\sigma_z^{(i)} \otimes \sigma_z^{(i+1)}$. This is the minimal entangling primitive that, combined with arbitrary single-qubit rotations, still spans $\mathfrak{su}(N)$ under iterated Lie brackets [32, 36]. The remaining 14 directions of $\mathfrak{su}(4)_{i, i+1}$ are not implemented as native gates: they are recovered by composing ZZ rotations with single-qubit ones, at the cost of additional circuit depth.

Under this restriction, the native gate set becomes

$$\mathcal{S} = \left\{ e^{-i\theta \sigma_a^{(i)}}, e^{-i\phi \sigma_z^{(i)} \otimes \sigma_z^{(i+1)}} \right\}, \quad (22)$$

with $a \in \{x, y, z\}$ and $\theta, \phi \in \mathbb{R}$ and whose associated Lie algebra is

$$\mathfrak{g}_{ZZ} = \text{span}_{\mathbb{R}}\{i\sigma_a^{(i)}, i\sigma_z^{(i)} \otimes \sigma_z^{(i+1)}\}. \quad (23)$$

This contains $3N_q + (N_q - 1) = 4N_q - 1$ generators, compared to the $18N_q - 15$ generators of the full nearest-neighbor algebra \mathfrak{g} in Eq. (19), reducing the number of native two-qubit parameters from $15(N_q - 1)$ to $4N_q - 1$. Despite this reduction, universality is preserved: the missing two-qubit interaction types are systematically recovered by commuting ZZ generators with single-qubit ones, so that $\overline{\mathfrak{g}_{ZZ}}$ still closes to the full $\mathfrak{su}(N)$ [35, 36],

$$\overline{\text{Lie}(\mathfrak{g}_{ZZ})} = \mathfrak{su}(N), \quad (24)$$

and therefore \mathcal{S} constitutes a universal gate set. An explicit Pauli-string example showing how a YZ -type term is generated from ZZ and single-qubit rotations is given in Appendix B.

Based on both the chain-topology and the ZZ -only assumptions, the elementary building block we adopt is therefore

$$H_{\text{chain}} = \underbrace{\sum_{i=1}^{N_q} \sum_{a \in \{X, Y, Z\}} \gamma_a^{(i)} \sigma_a^{(i)}}_{\text{1-qubit: } 3N_q \text{ terms}} + \underbrace{\sum_{i=1}^{N_q-1} \gamma_{ZZ}^{(i, i+1)} \sigma_z^{(i)} \otimes \sigma_z^{(i+1)}}_{\text{ZZ-only: } N_q-1 \text{ terms}}, \quad (25)$$

involving $4N_q - 1$ independent real parameters $\{\gamma_a^{(i)}, \gamma_{ZZ}^{(i, i+1)}\} \subset (-\pi, +\pi]$. By composing multiple layers of the form (25), any target unitary $U_{\text{target}} \in SU(N)$ can be approximated to arbitrary precision, at the cost of increased circuit depth [37, 38].

D. Continuous Family of Controls

In this section, we provide some examples of controls. This allows us not only to give a more realistic idea of what the controls used in this work look like, but also to show how their form depends continuously on the parameters of the generators.

Example of $SU(2)$ (1 qubit)

$$U = \exp\{i(\gamma_1 \sigma_x + \gamma_2 \sigma_y + \gamma_3 \sigma_z)\}, \quad (26)$$

with $\sigma_{x, y, z}$ the Pauli matrices.

Since:

$$e^{i\gamma_1 \sigma_x} = \begin{pmatrix} \cos \gamma_1 & i \sin \gamma_1 \\ i \sin \gamma_1 & \cos \gamma_1 \end{pmatrix}, \quad (27)$$

$$e^{i\gamma_2 \sigma_y} = \begin{pmatrix} \cos \gamma_2 & \sin \gamma_2 \\ -\sin \gamma_2 & \cos \gamma_2 \end{pmatrix}, \quad (28)$$

$$e^{i\gamma_3 \sigma_z} = \begin{pmatrix} e^{i\gamma_3} & 0 \\ 0 & e^{-i\gamma_3} \end{pmatrix}, \quad (29)$$

Introducendo per brevità $c_j \equiv \cos \gamma_j$ e $s_j \equiv \sin \gamma_j$,

$$U = e^{i\gamma_1 \sigma_x} e^{i\gamma_2 \sigma_y} e^{i\gamma_3 \sigma_z} = \begin{pmatrix} e^{i\gamma_3} (c_1 c_2 - i s_1 s_2) & e^{-i\gamma_3} (c_1 s_2 + i s_1 c_2) \\ e^{i\gamma_3} (i s_1 c_2 - c_1 s_2) & e^{-i\gamma_3} (c_1 c_2 + i s_1 s_2) \end{pmatrix} \quad (30)$$

This is the smooth manifold in which elements of $SU(2)$ lays. Hence, the associated controls $\epsilon_1(t)$ obtained with equation (4) will smoothly change with change of parameters $\gamma_1, \gamma_2, \gamma_3$.

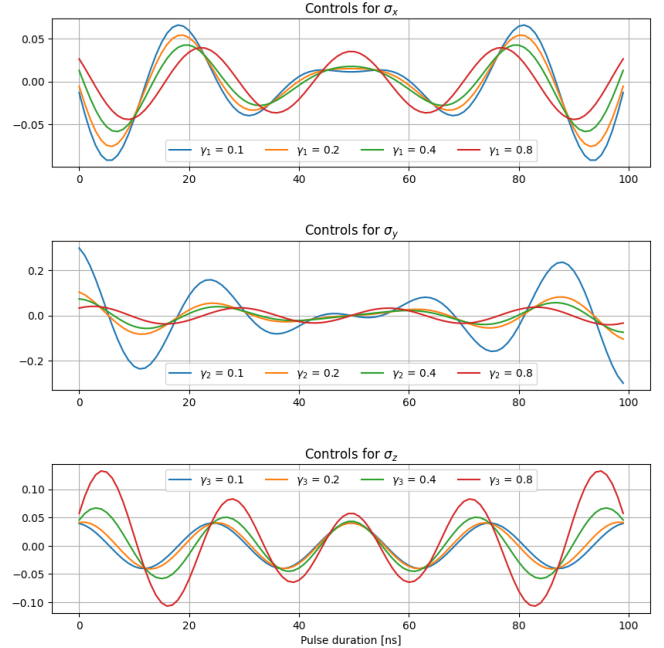


FIG. 1: Example of controls $\epsilon_1(t)$ for different values of the parameters $\gamma_1, \gamma_2, \gamma_3$ in the generator of $SU(2)$, as shown in the text. Small changes in the parameters lead to small changes in the controls, which is a consequence of the smooth manifold structure of $SU(2)$. In this work this feature is crucial to interpolate between controls.

In the σ_x we have the following matrices:

$$\gamma_1 = 0.1, \gamma_2 = 0, \gamma_3 = 0 \\ U = \begin{pmatrix} 0.9987 + 0.i & 0. - 0.0499i \\ 0. - 0.0499i & 0.9987 + 0.i \end{pmatrix}$$

$$\gamma_1 = 0.2, \gamma_2 = 0, \gamma_3 = 0 \\ U = \begin{pmatrix} 0.9950 + 0.i & 0. - 0.0998i \\ 0. - 0.0998i & 0.9950 + 0.i \end{pmatrix}$$

$$\gamma_1 = 0.4, \gamma_2 = 0, \gamma_3 = 0 \\ U = \begin{pmatrix} 0.9800 + 0.i & 0. - 0.1986i \\ 0. - 0.1986i & 0.9800 + 0.i \end{pmatrix}$$

$$\gamma_1 = 0.8, \gamma_2 = 0, \gamma_3 = 0 \\ U = \begin{pmatrix} 0.9210 + 0.i & 0. - 0.3894i \\ 0. - 0.3894i & 0.9210 + 0.i \end{pmatrix}$$

E. Quantum Systems simulation

It is well established that the propagators U of a quantum system belong to the unitary group $U(N)$ or, upon neglecting a global phase—which leaves the expectation values of all observables unchanged—to its subgroup, the special unitary group $SU(N)$ [39, 40]. The most immediate example, corresponding to $N = 2$, is provided by the Pauli matrices introduced above, which describe the interaction of a particle’s spin with an external electromagnetic field and equally characterize the rotations of a single qubit. More generally, for a quantum system whose Hilbert space is N -dimensional, the group $SU(N)$ describes the full set of admissible transformations of that closed quantum system.

In a quantum computing architecture, the only implementable operations are those belonging to the group $SU(N) = \bigotimes_{i=1}^n SU(2)$, where n denotes the number of qubits. The problem of simulating the dynamics of a quantum system with propagator $U_{\text{sys}} \in SU(N)$ on a quantum computer therefore reduces to finding an appropriate sequence of single- and multi-qubit operations, i.e. $SU(m)$ transformations, such that their combined action reproduces the effect of an arbitrary target unitary U_{sys} . In the framework of quantum optimal control, these operations are realized as optimized microwave pulse sequences that drive the qubit register into the desired target state.

A standard approach to quantum simulation consists of decomposing the system propagator as $U_{\text{sys}} = e^{-i \delta t H_{\text{sys}}}$ and determining the corresponding control pulses via an optimization algorithm, such as the one described in Sec. II A. A significant limitation of this approach emerges when the Hamiltonian—and consequently the propagator—are time-dependent, i.e., $U_{\text{sys}}(t) = e^{-i \delta t H_{\text{sys}}(t)}$. In this case, a new set of control pulses must be independently optimized for each time step $U_{\text{sys}}(t_i)$ of the simulation [16, 17]. Furthermore, quantum simulations typically require computing the time evolution from a large number of distinct initial configurations in order to fully characterize the system, which further multiplies the number of required optimization runs. Taken together, these factors can rapidly offset the benefits of an optimal control strategy.

III. LIE ALGEBRA BASED CONTROL PULSE RECONSTRUCTION

For a quantum device whose drift and control Hamiltonians close, under iterated Lie brackets, on the full algebra $\mathfrak{su}(N)$, any unitary $U \in SU(N)$ can in principle be realized by a suitable control sequence $\epsilon(t)$ [34–36]. Such a sequence is accessible to standard optimization procedures (e.g. GRAPE). Conversely, the propagators of every closed quantum system whose Hilbert space has dimension N belong to $SU(N)$: the abstract group $SU(N)$ thus provides a system-agnostic parametrization of all

target unitaries of fixed dimension.

The method we propose exploits this correspondence. Given a hardware register of N_q qubits – for which $N = 2^{N_q}$ – we sample a representative set of propagators $\{U_j\} \subset SU(N)$ via Eq. (25), compute the corresponding GRAPE-optimized controls once and for all, and train a feed-forward neural network to learn the map $U \mapsto \epsilon(t)$. Once trained, the network returns the controls for any new target $\tilde{U} \in SU(N)$ at neural network inference cost, including propagators originating from physical systems other than the qubit register itself, provided their Hilbert space dimension matches $N = 2^{N_q}$.

The sampling of the group elements builds on the Lie algebra framework summarized in Sec. II C: we use the parametrization

$$U = \exp(-iH_{\text{chain}}), \quad (31)$$

where H_{chain} is the chain Hamiltonian of Eq. (25) and the coefficients $\{\gamma_a^{(i)}, \gamma_{ZZ}^{(i,i+1)}\}$ are the free real parameters labeling points of $SU(N)$.

The optimal-control problem of Eq. (7) is solved here for the specific qubit Hamiltonian of Eq. (8), whose control term $H_{\text{ctrl}}(t)$ is parametrized by the in-phase and quadrature envelopes $\Omega_x(t)$, $\Omega_y(t)$ of Eq. (11). For this reason the controls reconstructed by LA-CPR are denoted $\Omega_x(t)$, $\Omega_y(t)$, rather than the generic $\epsilon_k(t)$ of Sec. II A.

The full *Lie Algebra-based Control Pulse Reconstruction* (LA-CPR) procedure proceeds in four steps:

1. **Sampling.** Build a dataset of propagators $\{U_j\}$ from Eq. (31), drawing each coefficient $\gamma_a^{(i)}$, $\gamma_{ZZ}^{(i,i+1)}$ independently from the uniform distribution on $[-z, z]$, with fixed $z \in \mathbb{R}$.
2. **Optimization.** For each U_j , run GRAPE to obtain the in-phase and quadrature control envelopes $\Omega_x^j(t)$ and $\Omega_y^j(t)$, yielding the paired dataset $\{(U_j, \Omega_x^j, \Omega_y^j)\}$.
3. **Training.** Train two feed-forward neural networks — one for $\Omega_x(t)$, one for $\Omega_y(t)$ — on the dataset, so that each network learns the map $U \mapsto \Omega_a(t)$ with $a \in [x, y]$.
4. **Inference.** For any new target $\tilde{U} \notin \{U_j\}$, the trained networks return the reconstructed controls $\tilde{\Omega}_x(t)$, $\tilde{\Omega}_y(t)$ in a single forward pass, with no further GRAPE optimization required.

The GRAPE runs in step 2 are warm-started from the controls associated with the propagator obtained by setting all coefficients of H_{chain} to $\gamma_a^{(i)}, \gamma_{ZZ}^{(i,i+1)} = 0.1$. This choice weights every generator equally and provides a balanced reference unitary from which the rest of the dataset is reconstructed.

Implementation details of LA-CPR and the neural-network architecture are deferred to Appendix C.

1. Datasets

An appropriate dataset is essential for LA-CPR to have good performance. As specified in Step 1 of the method, the Lie algebra coefficients $\{\gamma_a^{(i)}, \gamma_{ZZ}^{(i,i+1)}\}$ entering Eq. (31) are drawn independently from a uniform distribution on the interval $[-z, z]$. The choice of z controls the region of the group manifold explored by the dataset: a wider interval encompasses a larger and more diverse set of group elements, while a narrower one restricts the sample to transformations closer to the identity.

In principle, setting $z = \pi$ already covers all elements of the group. However, the sheer number of distinct unitaries in such a range can make the reconstruction task too demanding for LA-CPR, as shown in the following. For this reason, we restrict our analysis to three narrower intervals, corresponding to $z = \pi/8, \pi/4, \text{ and } \pi/2$, which probe regions of increasing extent around the identity.

Regarding the temporal structure of the control pulses, short pulses are preferable as they keep the manipulation time well below the coherence times of the qubits. On the other hand, encoding all the information required for a faithful transformation – especially for larger qubit registers – may require a minimum pulse duration. As a compromise between these two requirements, we fix the pulse duration to $\tau = 150$ ns for all datasets considered in this work.

IV. RESULTS

We evaluate LA-CPR on quantum systems of $N_q = 2, 3, 4$ qubits, each described by Eq. (8), using the three datasets ($z = \pi/8, \pi/4, \pi/2$) introduced in the previous section. This setup lets us probe how the performance of the method depends both on the system size and on the extent of the explored region of the group manifold. The full list of numerical parameters used in the simulations, including the qubit frequencies, the coupling strengths and the control sampling frequency, is reported in Tab. III.

The quality of the control pulses reconstructed by LA-CPR is assessed through the *fidelity* (Eq. (5)) between the target and the reconstructed propagators. Given a target propagator \tilde{U} from the test set, the trained neural networks of LA-CPR method return the control fields $\Omega_x(t), \Omega_y(t)$, from which the reconstructed propagator U_{recon} is obtained as the discretized, time-ordered evolution

$$U_{\text{recon}} = \mathcal{T} \exp \left[-i \left(H_0 + \sum_{j=1}^{N_t} H_{\text{ctrl}}(t_j) \right) \delta t \right], \quad (32)$$

where $H_0 = H_{\text{drift}} + H_{\text{int}}$ (Eqs. (9)–(10)) is the time-independent part and $H_{\text{ctrl}}(t_j) = H_{\text{ctrl}}(\Omega_x(t_j), \Omega_y(t_j))$ is the control term of Eq. (11) evaluated on the reconstructed pulses at the N_t discretization times t_j , with

TABLE III: Numerical parameters used in the simulations.

Parameter	Symbol	Value	Unit
<i>Time Parameters</i>			
Pulse duration	τ	150	ns
Sampling frequency	f_s	2.0	GHz
Number of time steps	$N_t = \tau f_s$	300	–
Time step	$\delta t = \tau/N_t$	0.5	ns
<i>Cavity Parameters</i>			
Cavity frequency	ω_c	$2.5 \times 2\pi$	GHz
Drive frequency	ω_d	$\frac{1}{N_q} \sum_{i=0}^{N_q-1} \omega_i$	GHz
<i>Qubit Frequencies</i>			
Qubit 0	ω_0	$1.0 \times 2\pi$	GHz
Qubit 1	ω_1	$1.1 \times 2\pi$	GHz
Qubit 2	ω_2	$1.2 \times 2\pi$	GHz
Qubit 3	ω_3	$1.3 \times 2\pi$	GHz
<i>Coupling Strengths</i>			
Coupling qubits 0–1	J_{01}	$0.035 \times 2\pi$	GHz
Coupling qubits 1–2	J_{12}	$0.040 \times 2\pi$	GHz
Coupling qubits 2–3	J_{23}	$0.045 \times 2\pi$	GHz

time step δt (see Tab. III). The reconstruction quality is then quantified by the fidelity $\mathcal{F}(\tilde{U}, U_{\text{recon}})$.

1. Graphical insight: control pulse and its spectrum

Prior to the quantitative analysis of the LA-CPR method, we present a qualitative examination of a representative control pulse. Figure 2 shows an example of the control field $\Omega_x(t)$ for a 3-qubit system with $z = \pi/4$. The upper panel displays the exact control in the time domain alongside its LA-CPR reconstruction, with the corresponding reconstruction fidelity indicated in the inset. The lower panel presents the frequency spectra of both the exact and reconstructed controls.

Several features of the spectrum are noteworthy. A peak at low frequencies (~ 0.03 GHz) corresponds to the qubit–qubit interaction frequencies listed in the Tab. III which in fact are around 35 MHz. Additional peaks above 1 GHz are associated with the individual qubit transition frequencies. Finally, a peak near 3 GHz is identified as a harmonic artifact introduced by the optimizer due to the finite temporal discretization of the control pulse; its frequency is approximately twice the mean qubit frequency of ~ 1.5 GHz, consistent with a second-order harmonic.

2. Fidelity and dataset dimension

Figure 3 shows the average fidelity the LA-CPR method reach on test dataset as a function of the training dataset size on which is trained,

of sampling parameter z and of systems number of qubits N_q . The upper row reports the fidelity curves with the corresponding standard deviations as function of the dataset size, while the lower row shows the same information rearranged as heatmaps over the (dataset size, N_q)

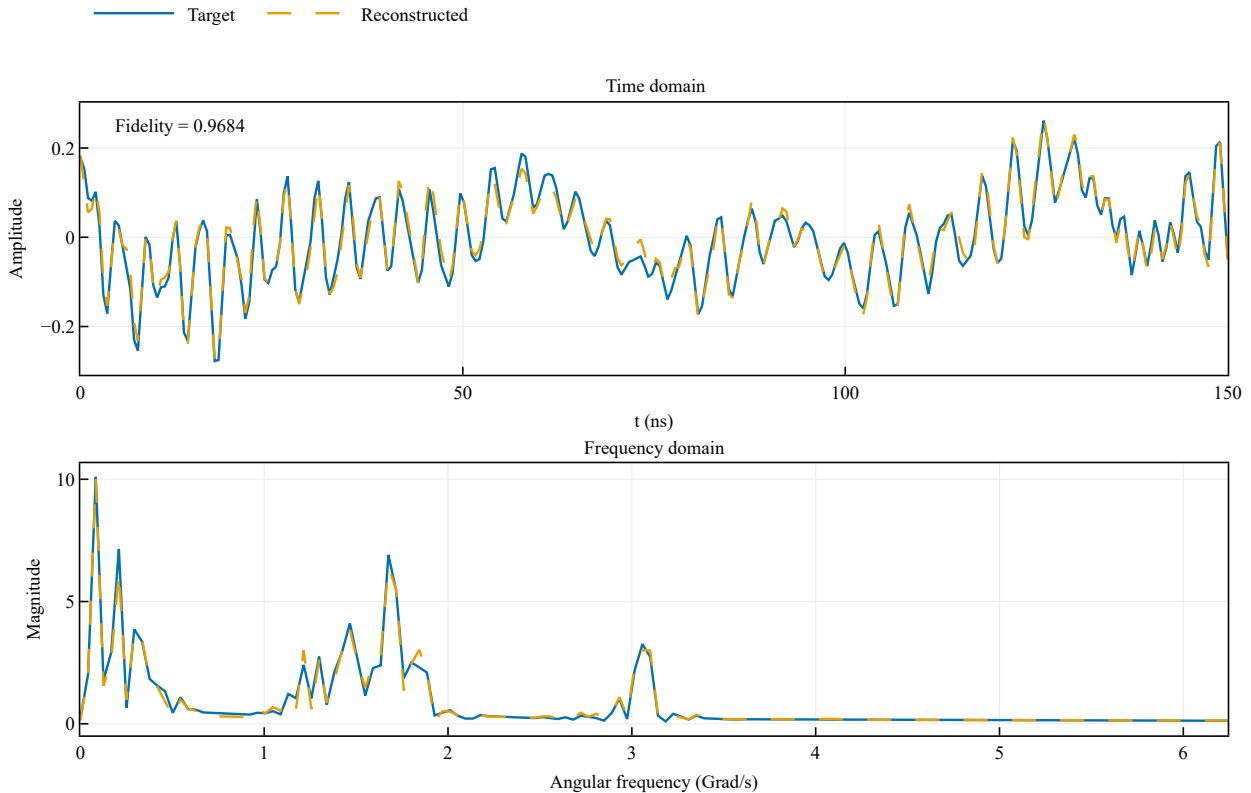


FIG. 2: Representative example of the control field $\Omega_x(t)$ reconstructed by the LA-CPR method for a 3-qubit system with $z = \pi/4$. *Upper panel:* time-domain profile of the exact (target) control and its LA-CPR reconstruction; the inset reports the corresponding fidelity. *Lower panel:* frequency spectra of both signals. The peak at ~ 0.03 GHz reflects the qubit-qubit interaction frequencies (see Tab. III); peaks above 1 GHz correspond to individual qubit transition frequencies; the feature near 3 GHz is a second-order harmonic artifact introduced by the optimizer due to the finite temporal discretization of the pulse.

plane, which makes the joint dependence on dataset size and system dimension immediately visible. In all configurations, the fidelity increases monotonically with the number of training samples and tends to saturate beyond approximately 10^4 elements, beyond which additional data yields only marginal improvement. This behavior is consistent with the well-known generalization properties of neural networks, where performance improves with training data but eventually reaches a regime of diminishing returns.

As expected, larger values of z lead to a systematic degradation of the fidelity. A wider sampling interval $[-z, z]$ covers a larger and more diverse region of the group manifold $SU(N)$, making the reconstruction task harder: the neural network must learn to interpolate across a more heterogeneous set of propagators, which reduces the precision of the generalization. This effect is particularly evident when comparing the $z = \pi/8$ and $z = \pi/2$ panels, where the latter shows a markedly lower fidelity across all dataset sizes and qubit numbers.

A similar degradation is observed as the number of qubits N_q increases. At fixed z and dataset size, the fi-

delity decreases monotonically when moving from $N_q = 2$ to $N_q = 4$, as clearly visible in the heatmaps of the lower row. This trend is consistent with the exponential growth of the group dimension, $\dim SU(2^{N_q}) = 4^{N_q} - 1$: realizing target unitaries on larger registers requires control pulses with a richer time structure, and the network must therefore interpolate the map $U \mapsto \Omega_{x,y}(t)$ over a higher-dimensional and more intricate landscape, which is intrinsically harder to learn from a finite training set.

These results indicate that, in practical applications of the LA-CPR method, one should prefer sampling regions close to the identity of the Lie group, i.e. small values of z , to obtain high-fidelity reconstructions without requiring excessively large datasets.

A. Comparison with standard gate decompositions

To provide a meaningful benchmark for our Lie-algebra-based quantum optimal control (QOC) reconstruction method, we evaluate the cost of implementing the same target unitaries through standard gate de-

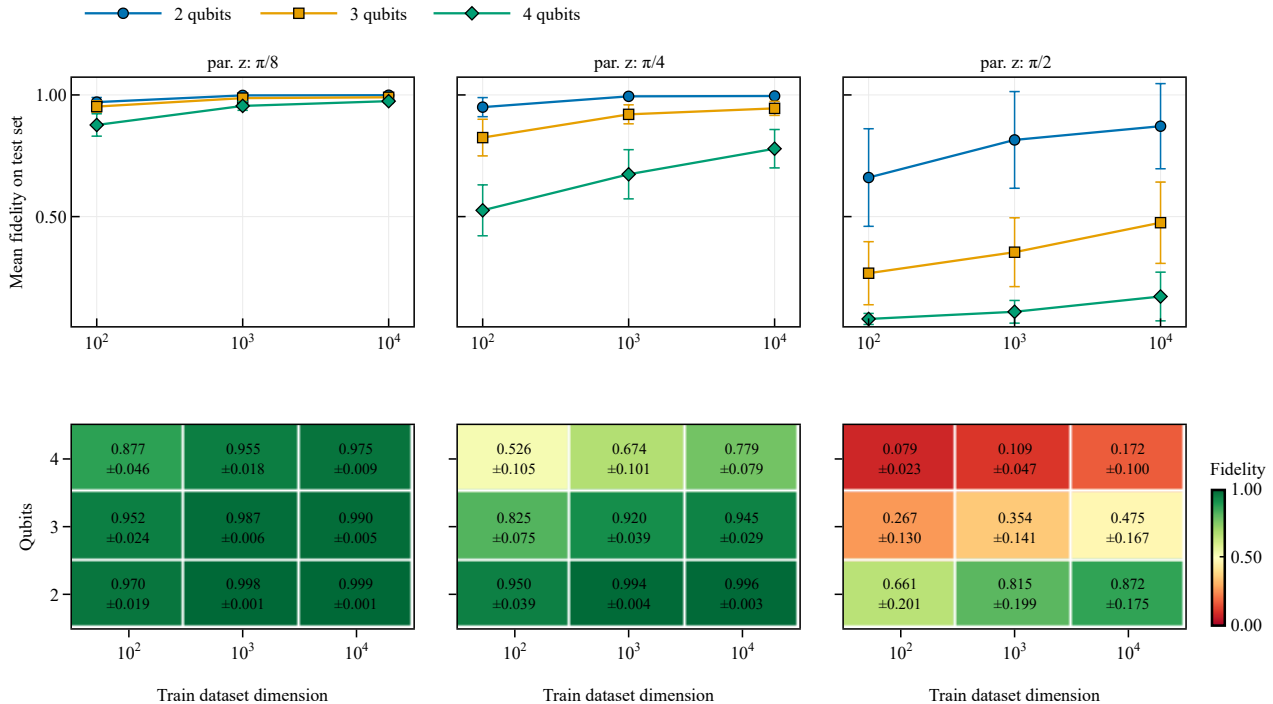


FIG. 3: Average fidelity of the LA-CPR method as a function of the training dataset size, for $z = \pi/8$ (left), $z = \pi/4$ (center), and $z = \pi/2$ (right). *Upper row*: mean fidelity on the test set versus training dataset dimension, with curves for $N_q = 2, 3, 4$ qubits; error bars indicate one standard deviation across independent training runs. *Lower row*: heatmaps of the same data, where each cell reports the mean fidelity \pm one standard deviation as a function of the training dataset dimension ($10^2, 10^3, 10^4$) and the number of qubits ($N_q = 2, 3, 4$); the color scale spans fidelities from 0 to 1 and provides a direct visualization of the joint dependence on dataset size and system dimension. In all cases the fidelity increases monotonically with the dataset size and saturates beyond approximately 10^4 elements. Larger values of z makes the reconstruction task progressively harder for the neural network, resulting in systematically lower fidelities.

composition as performed by a state-of-the-art quantum compiler. Specifically, for each system size $N \in \{2, 3, 4\}$ qubits, a representative target unitary is drawn at random from the set of propagators generated by the physical Hamiltonian of the system, and decomposed into the native gate set $\{\text{RZ}, \sqrt{X}, X, \text{CNOT}\}$ using the Qiskit transpiler at optimization level 3. For each decomposed circuit we record the following figures of merit: the total gate count, further broken down into the number of single-qubit gates (n_{1q}) and two-qubit gates (n_{2q}); the circuit depth, defined as the length of the longest critical path through the circuit when gates acting on disjoint qubits are parallelized; the estimated execution time T , defined as

$$T = n_{1q} \bar{t}_{1q} + n_{2q} \bar{t}_{2q}, \quad (33)$$

where $\bar{t}_{1q} = 10$ ns and $\bar{t}_{2q} = 50$ ns are the average durations of single- and two-qubit gates, respectively; and the estimated circuit fidelity F , defined as the product of the average per-gate fidelities over all gates in the circuit,

$$F = \bar{F}_{1q}^{n_{1q}} \bar{F}_{2q}^{n_{2q}}, \quad (34)$$

with $\bar{F}_{1q} = 0.9996$ and $\bar{F}_{2q} = 0.9950$. These quantities, summarised in Table IV, serve as a reference against which the resource requirements of our method can be compared.

TABLE IV: Gate decomposition of random unitaries for $N_q = 2, 3, 4$ qubits, compared with the LA-CPR reconstruction fidelity at $z = \pi/4$.

N_q	Total gates	1q gates	2q gates	Depth	Time [ns]	Decomp. fidelity	LA-CPR fidelity ($z = \pi/4$)
2	17	15	2	10	250.0	0.9841	0.996
3	95	78	17	63	1630.0	0.8901	0.945
4	491	405	86	300	8350.0	0.5526	0.779

More broadly, this comparison underscores a general advantage of control-based approaches over standard gate-decomposition pipelines, of which LA-CPR is one particular instance. By synthesizing complex unitaries directly as continuous control pulses, the physical execution time scales far more favorably with N_q than the rapidly growing circuit depths produced by compilation

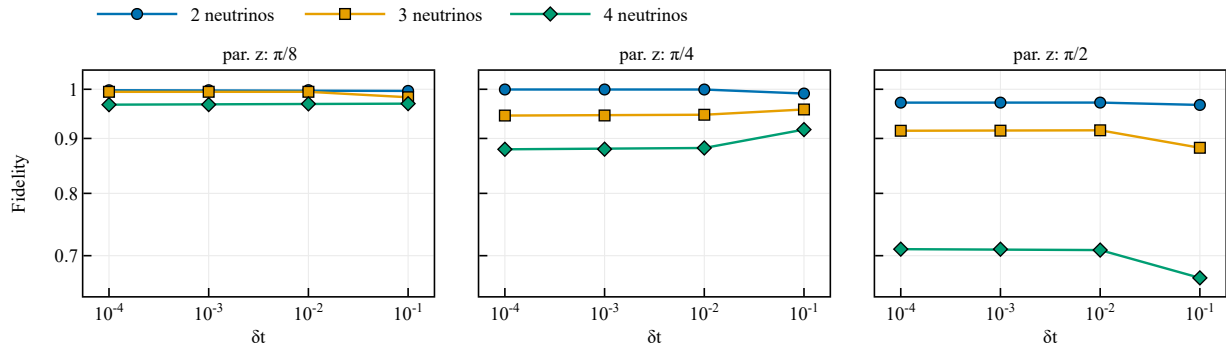


FIG. 4: Reconstruction fidelity of the LA-CPR method for the neutrino Trotter propagator $U_{\text{neutr}} = e^{-i\delta t H_{\text{neutr}}}$, shown as a function of the time step δt and the number of neutrinos N_n , for $z = \pi/8$ (left), $z = \pi/4$ (center), and $z = \pi/2$ (right). All models are trained on a dataset of 20000 elements. The fidelity decreases systematically with both δt and z : larger time steps displace the target propagators away from the group identity, while larger values of z broaden the training distribution, both increasing the difficulty of the reconstruction task.

into a discrete native gate set, which in this benchmark inflate from 250 ns at $N_q = 2$ to 8350 ns at $N_q = 4$. In the context of Trotterized quantum simulation, this allows each propagator $e^{-iH\delta t}$ to be implemented as a single pulse rather than as a long sequence of native gates, relaxing the pressure to slice δt too finely in order to keep the full evolution within the coherence window of present-day qubits.

V. PHYSICAL APPLICATION: SIMULATION OF NEUTRINO COLLECTIVE OSCILLATIONS

While the previous section assessed the LA-CPR method on random propagators, the primary motivation of this work is the efficient reconstruction of control pulses for propagators arising from the dynamics of physical quantum systems. In general, the LA-CPR method cannot reconstruct arbitrary propagators, since the sampling of the lie algebra parameters is restricted to the interval $[-z, z] \subsetneq [-\pi, \pi]$, confining the training distribution to a neighborhood of the group identity. This limitation is, however, naturally compatible with Trotterized real-time evolution, which is a standard technique in quantum simulation. In the Trotter decomposition, the full time-evolution operator is factored into short-time steps:

$$U(T) \approx \prod_{t=0}^T e^{-iH_{\text{sys}}(t)\delta t} = U_T U_{T-1} \cdots U_1 U_0, \quad (35)$$

where T denotes the total evolution time.

In the limit $\delta t \rightarrow 0$, each factor $U_i \rightarrow \mathbb{I}$; consequently, by reducing δt , the individual Trotter propagators can be confined to an arbitrarily small neighborhood of the identity in the Lie group. The LA-CPR method, whose

training set is constructed precisely from such a neighborhood, is therefore directly applicable in this regime.

As a concrete test case, we consider the collective flavor oscillations of neutrinos arising from forward neutrino-neutrino scattering, following the formulation of Refs. [14, 15]. Neutrinos are approximated as two-flavor particles, with the electron flavor ν_e and a single effective heavy flavor ν_x (representing a combination of the μ and τ flavors). Under this approximation, the flavor state of each neutrino, $|\psi_{\text{neut}}\rangle = \alpha|\nu_e\rangle + \beta|\nu_x\rangle$, maps naturally onto a single-qubit state $|\psi_q\rangle = a|0\rangle + b|1\rangle$. Each neutrino state therefore spans an $SU(2)$ space, and a system of N_n neutrinos belongs to $SU(2^{N_n})$, which makes it a well-suited benchmark for the LA-CPR method. The flavor Hamiltonian decomposes into a one-body term H_1 , accounting for vacuum mixing, and a two-body neutrino-neutrino interaction term H_2 , generated by forward scattering:

$$H_{\text{neutr}} = \underbrace{\sum_{i=1}^{N_n} \mathbf{b} \cdot \boldsymbol{\sigma}_i}_{H_1} + \underbrace{\sum_{i=1}^{N_n} \sum_{j=i+1}^{N_n} J_{ij} \boldsymbol{\sigma}_i \cdot \boldsymbol{\sigma}_j}_{H_2}, \quad (36)$$

where bold symbols denote 3-dimensional vectors, N_n is the number of neutrinos, and $\boldsymbol{\sigma}_i = (\sigma_i^{(x)}, \sigma_i^{(y)}, \sigma_i^{(z)})$ collects the Pauli matrices acting on the i -th neutrino, embedded in the full Hilbert space as $\sigma_i^{(\alpha)} = \mathbb{I}_1 \otimes \cdots \otimes \mathbb{I}_{i-1} \otimes \sigma^{(\alpha)} \otimes \mathbb{I}_{i+1} \otimes \cdots \otimes \mathbb{I}_{N_n}$. Following Ref. [15], the vacuum mixing vector is taken constant across N_n and equal to $\mathbf{b} = (0.38019, 0, -0.92491)$. The neutrino-neutrino couplings follow $J_{ij} = 1 - \cos\theta_{ij}$ with geometric angles $\theta_{ij} = \arccos(0.9)|i-j|/(N_n-1)$, so J_{ij} depends only on the pair distance $|i-j|$ and on N_n . The resulting values are summarised in Table V.

We benchmark the LA-CPR method on the single-step

TABLE V: Neutrino-neutrino couplings J_{ij} entering H_{neutr} , listed by pair distance $|i - j|$ for $N_n = 1, 2, 3, 4$.

N_n	$ i - j $	θ_{ij} [rad]	J_{ij}
1	–	–	–
2	1	0.4510	0.1000
3	1	0.2255	0.0253
3	2	0.4510	0.1000
4	1	0.1503	0.0113
4	2	0.3007	0.0449
4	3	0.4510	0.1000

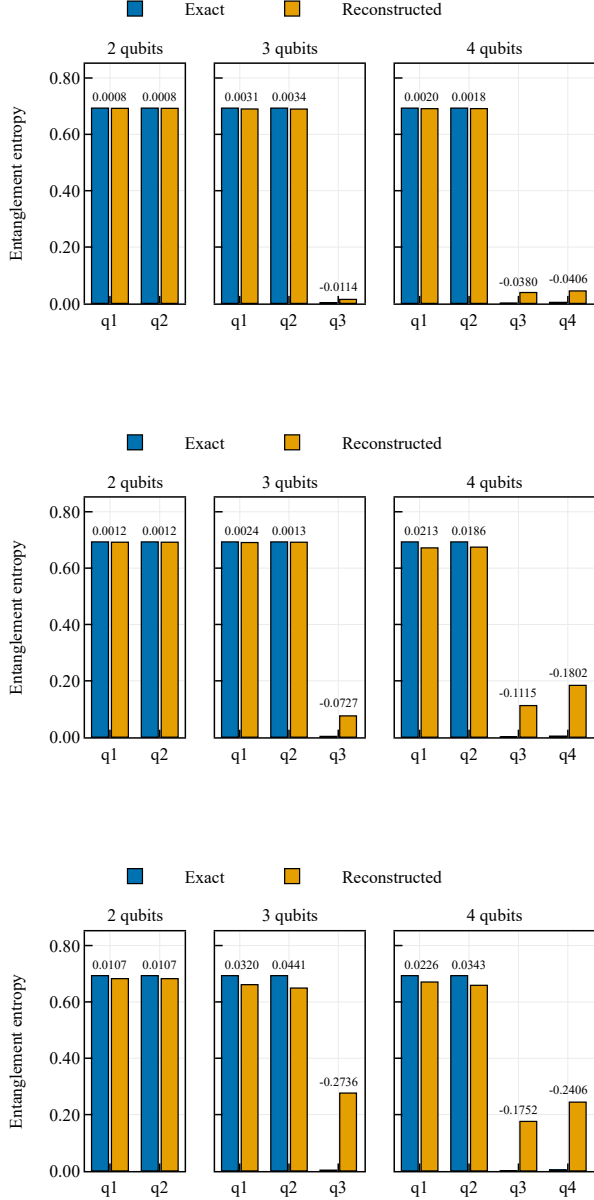


FIG. 5: Single-qubit von Neumann entropy S_k of the output state $|\psi\rangle = U|\psi_0\rangle$ for the exact (solid) and reconstructed (dashed) neutrino propagators, shown for $N_n = 2, 3, 4$ neutrinos and $z = \pi/8$ (top), $z = \pi/4$ (middle), and $z = \pi/2$ (bottom). The number over the bars represent the differences between them.

The exact and reconstructed entropy profiles are in close agreement for small z , while the discrepancy grows with increasing z , mirroring the trend observed in the gate fidelity and confirming that reconstruction accuracy degrades as the training distribution broadens.

Trotter propagator:

$$U_{\text{neutr}} = e^{-i\delta t H_{\text{neutr}}}, \quad (37)$$

for $N_n = 2, 3, 4$ neutrinos, whose propagators belong to $SU(4)$, $SU(8)$, and $SU(16)$, respectively. For

each system size, the time step is varied over $\delta t \in \{10^{-4}, 10^{-3}, 10^{-2}, 10^{-1}\}$, so as to probe identity neighborhoods of progressively increasing width. The results are presented in Fig. 4, where each panel corresponds to a fixed value of z and shows the reconstruction fidelity as function of δt with a line for every number of neutrinos N_n . All models trained on a dataset of 10 000 elements. A systematic decrease in fidelity with increasing δt and z is observed. This behavior is consistent with the results of the previous section: larger values of z broaden the training distribution, increasing reconstruction difficulty, while larger δt displaces the target propagators further from the group identity, placing them increasingly outside the region for which the method was trained.

To further validate the reconstruction at the state level, we assess whether the reconstructed controls faithfully reproduce the entanglement structure generated by the exact neutrino propagators. We prepare the input state $|\psi_0\rangle = (|10\dots 0\rangle + |01\dots 0\rangle)/\sqrt{2}$, a single-excitation superposition across the first two qubits, and evolve it under both the exact and reconstructed unitary operators. For each output state $|\psi\rangle = U|\psi_0\rangle$, we compute the single-qubit von Neumann entropy $S_k = -\text{Tr}[\rho_k \log_2 \rho_k]$, where $\rho_k = \text{Tr}_{\neq k}[|\psi\rangle\langle\psi|]$ is the reduced density matrix of qubit k . The results are shown in Fig. 5 for $N_n = 2, 3, 4$ neutrinos and the three values of z considered throughout this work. For $z = \pi/8$, the exact and reconstructed entropy profiles agree closely across all system sizes, confirming that the reconstructed controls faithfully capture the entanglement dynamics of the neutrino propagators. As z increases, the agreement progressively deteriorates, consistent with the decrease in gate fidelity observed in Fig. 4: a broader training distribution reduces reconstruction accuracy and, consequently, the ability of the reconstructed controls to reproduce the correct entanglement structure. This state-level analysis provides an independent validation of the reconstruction quality, complementary to the average gate fidelity \bar{F} . It is also worth emphasizing that the neural networks were trained exclusively on randomly sampled propagators and were never exposed to the neutrino propagators during training.

These results suggest that the LA-CPR method can effectively reconstruct the control pulses for unitaries in $SU(N)$ on N_q qubits, at least within the regime of sufficiently small Trotter steps a condition naturally met in

Trotterized quantum simulation.

VI. CONCLUSIONS

We have introduced the Lie Algebra-based Control Pulse Reconstruction (LA-CPR) method, a hybrid approach that combines the mathematical structure of Lie groups with the generalization capabilities of feed-forward neural networks to address one of the central bottlenecks in quantum optimal control: the need to independently re-optimize control pulses for every new target propagator.

The key insight underlying LA-CPR is that all propagators of an N_q -qubit system belong to $SU(N)$, a compact Lie group that can be systematically sampled via its associated Lie algebra. By exploiting the Pauli tensor basis decomposition of $\mathfrak{su}(N)$ and restricting the native gate set to a linear chain topology with Ising ZZ coupling – a physically well-motivated simplification for superconducting architectures – we obtain a compact and hardware-consistent parametrization of the full group. A dataset of GRAPE-optimized control pulses is computed once for a representative sample of group elements drawn from a neighborhood of the identity, and two feed-forward neural networks are trained to map each propagator to its corresponding $\Omega_x(t)$ and $\Omega_y(t)$ control envelopes.

The numerical experiments on systems of $N_q = 2, 3, 4$ qubits demonstrate that LA-CPR achieves high reconstruction fidelity with training datasets of approximately 10^4 elements, beyond which additional samples yield only marginal improvement. As expected, restricting the sampling interval $[-z, z]$ to smaller values of z – corresponding to a tighter neighborhood of the group identity – systematically improves reconstruction quality, since the neural network is required to interpolate over a more homogeneous region of the group manifold.

A comparison with standard gate-decomposition pipelines further highlights a structural advantage of control-based methods, of which LA-CPR is one instance: synthesizing each target unitary as a single continuous pulse achieves higher fidelities in much shorter physical times, relaxing the need for very small Trotter steps to stay within the coherence window of present-day qubits.

The application to neutrino collective oscillations provides a compelling proof of concept for the use of LA-CPR in quantum simulation. Despite the fact that the neural networks were trained exclusively on hardware-specific random propagators, the method successfully reconstructed control pulses for the physical Trotter propagators of $N_n = 2, 3, 4$ neutrino systems across a range of time steps, without any retraining or system-specific adaptation. This result confirms the key practical advantage of LA-CPR: a single offline training phase, tied to the hardware Hamiltonian rather than to any particular target system, produces a reusable model that can be deployed for any quantum simulation task on the same de-

vice. This makes LA-CPR particularly well suited to the simulation of many-body systems, where large ensembles of distinct propagators must be processed efficiently.

Looking ahead, several natural extensions of the method merit investigation. Scaling to larger qubit registers will require addressing the exponential growth of the input dimension and the increased diversity of the group manifold; techniques such as structured input representations, locality-aware network architectures, or hierarchical decompositions may prove beneficial in this regime. It would also be interesting to explore whether training on correlated, physically motivated datasets – rather than uniformly random samples – could improve fidelity for specific classes of target systems. Finally, a systematic study of the interplay between Trotter step size, sampling radius z , and reconstruction fidelity would help establish practical guidelines for deploying LA-CPR within larger quantum simulation workflows.

Appendix A: Pauli Basis Decomposition: $N_q = 3$

For $N_q = 3$, the algebra $\mathfrak{su}(8)$ has dimension $4^3 - 1 = 63$. The Hamiltonian expands as

$$H = \underbrace{\sum_{i=1}^3 \sum_a \gamma_a^{(i)} \sigma_a^{(i)}}_{\text{1-qubits: 9 terms}} + \underbrace{\sum_{i < j} \sum_{a,b} \gamma_{ab}^{(ij)} \sigma_a^{(i)} \otimes \sigma_b^{(j)}}_{\text{2-qubits: 27 terms}} + \underbrace{\sum_{a,b,c} \theta_{abc} \sigma_a^{(1)} \otimes \sigma_b^{(2)} \otimes \sigma_c^{(3)}}_{\text{3-qubits: 27 terms}}. \quad (\text{A1})$$

TABLE VI: Pauli basis for $N_q = 3$, $\dim \mathfrak{su}(8) = 63$.

Locality	Operators	No. of terms
1-qubits	$\sigma_a^{(i)}, i \in \{1, 2, 3\}$	9
2-qubits	$\sigma_a^{(i)} \otimes \sigma_b^{(j)}, i < j$	27
3-qubits	$\sigma_a^{(1)} \otimes \sigma_b^{(2)} \otimes \sigma_c^{(3)}$	27
Total		63

Appendix B: Simplification of Lie Algebra

1. Chain topology simplification

We report here how the algebra \mathfrak{g} of Eq. (19) can generate the missing direction of $\mathfrak{su}(8)$ with commutators. We illustrate this with an explicit Pauli-string computation. Consider the generators.

$$\begin{aligned} A &= i(\sigma_z \otimes \sigma_x \otimes \mathbb{I}) \in \mathfrak{su}(4)_{12}, \\ B &= i(\mathbb{I} \otimes \sigma_x \otimes \sigma_z) \in \mathfrak{su}(4)_{23}. \end{aligned} \quad (\text{B1})$$

These correspond to nearest-neighbor interactions and are natively available. Their commutator is

$$\begin{aligned} [A, B] &= (i\sigma_z \sigma_x \mathbb{I})(i\mathbb{I} \sigma_x \sigma_z) - (i\mathbb{I} \sigma_x \sigma_z)(i\sigma_z \sigma_x \mathbb{I}) \\ &= -(\sigma_z \sigma_x \mathbb{I})(\mathbb{I} \sigma_x \sigma_z) + (\mathbb{I} \sigma_x \sigma_z)(\sigma_z \sigma_x \mathbb{I}) \\ &= -(\sigma_z \otimes \sigma_x^2 \otimes \sigma_z) + (\sigma_z \otimes \sigma_x^2 \otimes \sigma_z) \\ &= -2i(\sigma_z \otimes \mathbb{I} \otimes \sigma_z) + 2i(\sigma_z \otimes \mathbb{I} \otimes \sigma_z), \end{aligned} \quad (\text{B2})$$

which, after careful application of the Pauli identity $\sigma_x^2 = \mathbb{I}$ and the commutation relation $[iP, iQ] = -[P, Q]$, yields the non-trivial result

$$[A, B] \propto i(\sigma_z \otimes \mathbb{I} \otimes \sigma_z). \quad (\text{B3})$$

The operator $\sigma_z \otimes \mathbb{I} \otimes \sigma_z$ acts non-trivially on qubits 1 and 3 simultaneously, while being the identity on the mediating qubit 2. This is a *long-range* Pauli string—one that has no support in either $\mathfrak{su}(4)_{12}$ or $\mathfrak{su}(4)_{23}$ alone—and it lies outside the original generators of \mathfrak{g} . Repeating this procedure for all inequivalent pairs of nearest-neighbor Pauli strings, one systematically generates all $4^3 - 1 = 63$ independent traceless Pauli strings on three qubits.

2. ZZ coupling simplification

We show here how the restricted algebra

$$\mathfrak{g}_{ZZ} = \text{span}_{\mathbb{R}} \{ i\sigma_a^{(i)}, i\sigma_z^{(i)} \otimes \sigma_z^{(i+1)} \} \quad (\text{B4})$$

still closes to $\mathfrak{su}(N)$ under iterated Lie brackets, even though only one of the fifteen two-qubit generators of $\mathfrak{su}(4)_{i,i+1}$ is retained natively. The missing interaction types are recovered by commuting the ZZ generator with single-qubit rotations. For instance, the YZ -type term is obtained as

$$\begin{aligned} &[i\sigma_z^{(i)} \otimes \sigma_z^{(i+1)}, i\sigma_x^{(i)} \otimes \mathbb{I}^{(i+1)}] \\ &= -[\sigma_z^{(i)}, \sigma_x^{(i)}] \otimes \sigma_z^{(i+1)} \\ &= 2i\sigma_y^{(i)} \otimes \sigma_z^{(i+1)}, \end{aligned} \quad (\text{B5})$$

where we used $[\sigma_z, \sigma_x] = -2i\sigma_y$ and the mixed-product property of the tensor commutator. Analogous commutators with $\sigma_y^{(i)}$ or with operators on site $i+1$ generate the remaining XZ, ZX, ZY Pauli strings, and a further nested bracket between two such terms produces XX, YY, XY, YX couplings. Combined with the chain-topology construction of the previous subsection, this recovers all $4^{N_q} - 1$ traceless Pauli strings, establishing universality of the gate set \mathcal{S} .

Appendix C: LA-CPR Method technical details

a. LA-CPR Preparation

LA-CPR method requires a preparation phase before its actual use. Let's consider the $SU(N)$ group with its associated Lie algebra $\mathfrak{su}(N)$. We should:

1. Provide the experimental parameters of the device in use, i.e. the specific qubits Hamiltonian of Eq. (8).
2. Define the basis set $\{T_p\}$ of $\mathfrak{su}(N)$ as described in Sec. II C.
3. Compute the set of matrices $\{U_j\}$ via Eq. (31) sampling the parameters γ_l from a uniform distribution in the interval $[-z, z]$ with $z \in (0, \pi]$.
4. Compute the controls $\epsilon_j^k(t)$, using GRAPE algorithm, to solve the formal minimization problem of Eq. (7) for each U_j in the dataset. We thus obtain 2 datasets of controls representing $\Omega_x(t)$ and $\Omega_y(t)$ of the qubits systems Eq. (11).
5. Prepare the inputs and the outputs for the neural network. Since the neural network can only take vectors as inputs, each matrix U_j is flattened stacking the real and the imaginary part of the matrix in a single vector, i.e. $U_j^{flat} = [\text{Re } U_j^{1,1}, \dots, \text{Re } U_j^{N,N}, \text{Im } U_j^{1,1}, \dots, \text{Im } U_j^{N,N}]$. The

outputs instead are the controls themselves, which are already in the shape of single vectors.

- Define 2 feed-forward neural networks (FFNN), one for each output dataset, with an appropriate architecture. Train each FFNN to link U_j^{flat} to the corresponding control $\epsilon_j^k(t)$, i.e. $\epsilon_j^k = f_k(U_j^{flat})$.

b. LA-CPR Use

After the preparation phase, the use of LA-CPR method is straightforward.

- Take any arbitrary matrix $\tilde{U} \in SU(N)$ not in the training dataset.
- Flatten \tilde{U} in a vector, $\tilde{U} \rightarrow \tilde{U}^{flat}$.
- Insert \tilde{U}^{flat} in the 2 neural networks to obtain the corresponding controls $\tilde{\Omega}_a = f_a(\tilde{U}^{flat})$ for $a = x, y$.

The matrix \tilde{U} can be random or come from any quantum system we are interested in. The LA-CPR method is able to provide the control pulses for that specific propagator without performing an optimization and without requiring any knowledge of the quantum system itself.

c. Neural Networks

The neural networks used in this work are feedforward neural networks. The input, as specified in Step 5 of Sec. C 0 a, is the flattened representation U_j^{flat} of a propagator U_j in matrix form, and the output is the control pulse $\Omega_a(t)$ associated with that propagator. The network architecture consists of two hidden layers of 500 neurons each, with ReLU activation functions for the hidden layers. After each hidden layer, a Dropout layer with a rate of 0.1 is applied to reduce overfitting.

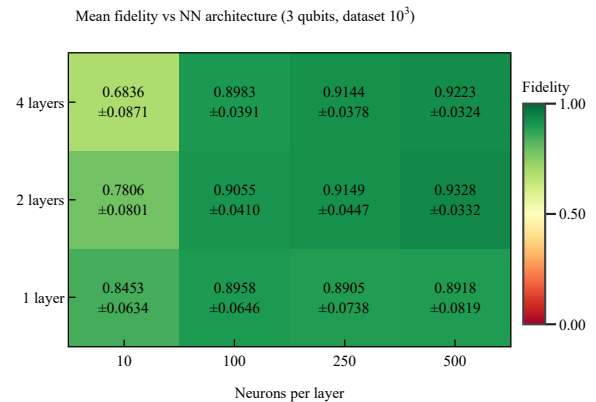
No normalization is applied to either the input or output data. The entries of the flattened propagator U_j^{flat} are naturally bounded in $[-1, 1]$, since the real and imaginary parts of a unitary matrix satisfy this constraint. Similarly, the control amplitudes $\Omega_a(t)$ oscillate within a comparable range, making explicit normalization unnecessary. Should different operating conditions require it, a normalization step could straightforwardly be introduced as a preprocessing stage.

Training is performed by minimizing a mean squared error (MSE) loss function using the Adam optimizer. The maximum number of epochs is set to 100, with an early stopping callback that halts training if the validation loss does not decrease for 6 consecutive epochs.

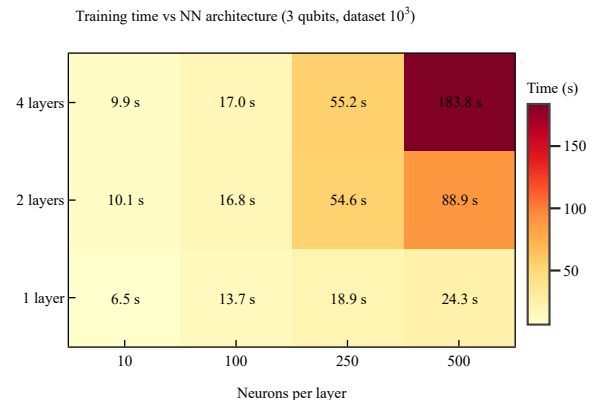
The choice of the network architecture – namely the number of hidden layers and neurons per layer – was determined through a grid search over a range of candidate configurations. The best-performing architecture was selected based on the validation MSE, and the results of this search are reported in Fig. 6.

Appendix D: Neural network architecture selection

Since there is no general theoretical recipe for choosing the best neural network architecture, the selection is carried out empirically through a grid search over depth and width. Networks with $N_l \in \{1, 2, 4\}$ hidden layers and $N_D \in \{10, 100, 250, 500\}$ neurons per layer are trained on a dataset of 10 000 elements with $z = \pi/4$ for 3 qubits, and evaluated on a test set of 200 elements. The results are shown in Fig. 6: the left panel reports the average reconstruction fidelity (with standard error) for each (N_l, N_D) combination, while the right panel shows the corresponding training time.



(a) Reconstruction fidelity.



(b) Training time.

FIG. 6: Grid search over neural network architectures: reconstruction fidelity (top) and training time (bottom) for all combinations of $N_l \in \{1, 2, 4\}$ hidden layers and layer width $N_D \in \{10, 100, 250, 500\}$, trained on 10 000 samples with $z = \pi/4$ for 3 qubits and evaluated on a 200-element test set.

The two panels together allow a joint assessment of accuracy and computational cost, facilitating the identification of an efficient architecture. As expected, increasing both the number of layers N_l and the layer width N_D generally improves the reconstruction fidelity. However, this gain is not linear: the marginal improvement in fi-

delity diminishes as the network grows larger, while the training time increases sharply. At the low end, networks with only $N_D = 10$ neurons per layer consistently underperform regardless of depth, indicating that this width is insufficient to capture the complexity of the mapping between unitary targets and control pulses. On the other hand, the largest configurations do not systematically outperform intermediate ones and can even degrade slightly, likely due to training difficulties and overfitting

on the finite dataset.

Based on this analysis, the architecture with $N_l = 2$ hidden layers and $N_D = 250$ neurons per layer is selected and used for all experiments in this work. This configuration achieves a favorable trade-off between fidelity (comparable to heavier architectures) and training cost (lower than heavier architectures). It should be noted that this choice is not universal and can be adjusted in each specific implementation depending on the available computational resources and the desired accuracy.

-
- [1] A. Barenco, C. H. Bennett, R. Cleve, D. P. DiVincenzo, N. Margolus, P. Shor, T. Sleator, J. A. Smolin, and H. Weinfurter, Elementary gates for quantum computation, *Phys. Rev. A* **52**, 3457 (1995).
- [2] A. Harrow and B. Recht, Efficient discrete approximations of quantum gates, *Journal of Mathematical Physics* **43** (2001).
- [3] S. Glaser, U. Boscain, T. Calarco, C. Koch, W. Köckenberger, R. Kosloff, I. Kuprov, B. Luy, S. Shemer, T. Schulte-Herbrüggen, D. Sugny, and F. Wilhelm, Training schrödinger’s cat: quantum optimal control, *The European Physical Journal D* **69** (2015).
- [4] J. Werschnik and E. Gross, Phd tutorial: Quantum optimal control theory, *Journal of Physics B-atomic Molecular and Optical Physics - J PHYS-B-AT MOL OPT PHYS* **40** (2007).
- [5] S. Lloyd, Universal quantum simulators, *Science* **273**, 1073 (1996).
- [6] A. M. Childs, Y. Su, M. C. Tran, N. Wiebe, and S. Zhu, Theory of Trotter error with commutator scaling, *Phys. Rev. X* **11**, 011020 (2021).
- [7] M. Bukov, A. G. R. Day, D. Sels, P. Weinberg, A. Polkovnikov, and P. Mehta, Reinforcement learning in different phases of quantum control, *Phys. Rev. X* **8**, 031086 (2018).
- [8] M. Y. Niu, S. Boixo, V. N. Smelyanskiy, and H. Neven, Universal quantum control through deep reinforcement learning, *npj Quantum Information* **5**, 33 (2019).
- [9] N. Khaneja, T. Reiss, C. Kehlet, T. Schulte-Herbrüggen, and S. J. Glaser, Optimal control of coupled spin dynamics: design of nmr pulse sequences by gradient ascent algorithms, *Journal of Magnetic Resonance* **172**, 296 (2005).
- [10] B. Rowland and J. Jones, Implementing quantum logic gates with gradient ascent pulse engineering: Principles and practicalities, *Philosophical transactions. Series A, Mathematical, physical, and engineering sciences* **370**, 4636 (2012).
- [11] T. Caneva, T. Calarco, and S. Montangero, Chopped random-basis quantum optimization, *Phys. Rev. A* **84**, 022326 (2011).
- [12] F. Sauvage and F. Mintert, Optimal control of families of quantum gates, *Phys. Rev. Lett.* **129**, 050507 (2022).
- [13] A. B. Magann, C. Arenz, M. D. Grace, T.-S. Ho, R. L. Kosut, J. R. McClean, H. A. Rabitz, and M. Sarovar, From pulses to circuits and back again: A quantum optimal control perspective on variational quantum algorithms, *PRX Quantum* **2**, 010101 (2021).
- [14] B. Hall, A. Roggero, A. Baroni, and J. Carlson, Simulation of collective neutrino oscillations on a quantum computer, *Phys. Rev. D* **104**, 063009 (2021).
- [15] V. Amitrano, A. Roggero, P. Luchi, F. Turro, L. Vespucci, and F. Pederiva, Trapped-ion quantum simulation of collective neutrino oscillations, *Physical Review D* **107** (2023).
- [16] P. Luchi, F. Turro, S. Quaglioni, X. Wu, V. Amitrano, K. Wendt, J. L. DuBois, and F. Pederiva, Control optimization for parametric hamiltonians by pulse reconstruction, *The European Physical Journal A* **59**, 196 (2023).
- [17] F. Turro, T. Chistolini, A. Hashim, Y. Kim, W. Livingston, J. M. Kreikebaum, K. A. Wendt, J. L. Dubois, F. Pederiva, S. Quaglioni, D. I. Santiago, and I. Siddiqi, Demonstration of a quantum-classical coprocessing protocol for simulating nuclear reactions, *Phys. Rev. A* **108**, 032417 (2023).
- [18] A. Blais, A. L. Grimsmo, S. M. Girvin, and A. Wallraff, Circuit quantum electrodynamics, *Rev. Mod. Phys.* **93**, 025005 (2021).
- [19] J. Koch, T. M. Yu, J. Gambetta, A. A. Houck, D. I. Schuster, J. Majer, A. Blais, M. H. Devoret, S. M. Girvin, and R. J. Schoelkopf, Charge-insensitive qubit design derived from the cooper pair box, *Phys. Rev. A* **76**, 042319 (2007).
- [20] A. Blais, R.-S. Huang, A. Wallraff, S. Girvin, and R. Schoelkopf, Cavity quantum electrodynamics for superconducting electrical circuits: An architecture for quantum computation, *Phys. Rev. A* **69** (2004).
- [21] A. Wallraff, D. I. Schuster, A. Blais, L. Frunzio, R.-S. Huang, J. Majer, S. Kumar, S. M. Girvin, and R. J. Schoelkopf, Strong coupling of a single photon to a superconducting qubit using circuit quantum electrodynamics, *Nature* **431**, 162 (2004).
- [22] M. Tavis and F. W. Cummings, Exact solution for an N -molecule—radiation-field Hamiltonian, *Phys. Rev.* **170**, 379 (1968).
- [23] J. Majer, J. M. Chow, J. M. Gambetta, J. Koch, B. R. Johnson, J. A. Schreier, L. Frunzio, D. I. Schuster, A. A. Houck, A. Wallraff, A. Blais, M. H. Devoret, S. M. Girvin, and R. J. Schoelkopf, Coupling superconducting qubits via a cavity bus, *Nature* **449**, 443 (2007).
- [24] A. Blais, J. Gambetta, A. Wallraff, D. I. Schuster, S. M. Girvin, M. H. Devoret, and R. J. Schoelkopf, Quantum-information processing with circuit quantum electrodynamics, *Phys. Rev. A* **75**, 032329 (2007).
- [25] P. Krantz, M. Kjaergaard, F. Yan, T. Orlando, S. Gustavsson, and W. Oliver, A quantum engineer’s guide to superconducting qubits, *App. Phys. Rev.* **6**, 021318 (2019).

- (2019).
- [26] A. Das and S. Okubo, *Lie groups and Lie algebras for physicists* (World Scientific, 2014).
- [27] M. A. Nielsen and I. L. Chuang, *Quantum Computation and Quantum Information* (Cambridge University Press, Cambridge, 2000).
- [28] K. Y. Chew, N. M. Shah, and K. T. Chan, Representation of $\mathfrak{su}(8)$ in Pauli basis, arXiv preprint [arXiv:2003.09192](https://arxiv.org/abs/2003.09192) (2020), arXiv:2003.09192 [quant-ph].
- [29] N. M. Shah, K. Y. Chew, and K. T. Chan, Algebraic representation of three qubit quantum circuit problems, *Malaysian Journal of Mathematical Sciences* **16**, 559 (2022).
- [30] T. Bröcker and T. tom Dieck, *Representations of Compact Lie Groups* (Springer, New York, 1985).
- [31] J. Zhang, J. Vala, S. Sastry, and K. B. Whaley, Geometric theory of nonlocal two-qubit operations, *Physical Review A* **67**, 042313 (2003).
- [32] N. Khaneja and S. J. Glaser, Cartan decomposition of $su(2^n)$ and control of spin systems, *Chemical Physics* **267**, 11 (2001).
- [33] R. Zeier and T. Schulte-Herbrüggen, Symmetry principles in quantum systems theory, *Journal of Mathematical Physics* **52**, 113510 (2011).
- [34] D. D'Alessandro, *Introduction to Quantum Control and Dynamics*, 2nd ed. (Chapman & Hall/CRC, 2021).
- [35] V. Jurdjevic and H. J. Sussmann, Control systems on Lie groups, *Journal of Differential Equations* **12**, 313 (1972).
- [36] V. Ramakrishna, M. V. Salapaka, M. Dahleh, H. Rabitz, and A. Peirce, Controllability of molecular systems, *Physical Review A* **51**, 960 (1995).
- [37] C. M. Dawson and M. A. Nielsen, The Solovay-Kitaev algorithm, *Quantum Information & Computation* **6**, 81 (2006), [arXiv:quant-ph/0505030](https://arxiv.org/abs/quant-ph/0505030).
- [38] J.-L. Brylinski and R. Brylinski, Universal quantum gates, in *Mathematics of Quantum Computation*, edited by R. Brylinski and G. Chen (Chapman & Hall/CRC, 2002) pp. 101–116.
- [39] H. Georgi and K. Jagannathan, *Lie Algebras in Particle Physics*, Vol. 50 (1982) pp. 1053–1053.
- [40] B. C. Hall, *Lie Groups, Lie Algebras, and Representations* (Springer Chams, 2013).